STM Images and Chemisorption Bond Parameters of Acetylene, Ethynyl, and Dicarbon Chemisorbed on Copper[†]

F. E. Olsson and M. Persson*

Department of Applied Physics, Chalmers/Göteborg University, S-41296 Göteborg, Sweden

N. Lorente

Laboratoire Collisions, Agrégats, Réactivité, UMR 5589, Université Paul Sabatier, 31062 Toulouse, Cedex France

L. J. Lauhon

Department of Chemistry and Chemical Biology, Harvard University, Cambridge, Massachusetts 02138-2902

W. Ho

Department of Physics and Astronomy and Department of Chemistry, University of California, Irvine, California 92697-4575

We present a combined theoretical and experimental study of chemisorption parameters and STM images for C_2H_2, C_2H, and C_2 on Cu(001). The geometric and electronic structure, and vibrational energies were obtained from density functional calculations. The calculated STM images were obtained from Kohn−Sham wave functions using the Tersoff and Hamann approximation. A dramatically enhanced resolution in the experimental STM images were obtained using a tip that was obtained by irreversible dissociation of H_2S. We find a near-quantitative agreement between experimental and calculated image for this tip and for a normal tip at appropriate tip−surface distances. An analysis shows that protrusions that appear in all images derive from adsorbate-induced resonances at the Fermi energy. All images also exhibit a wide depression that we attribute to the screening of the electronegative adsorbates by the metal conduction electrons.

1. Introduction

The scanning tunneling microscope (STM) provides a unique experimental analytical tool with atomic resolution for the study of chemisorption of single molecules and their interactions on surfaces. The interpretation of STM images is generally not straightforward because the resolved features do not simply reflect the positions of atoms in the chemisorbed molecule but rather the electronic states that contribute to the tunneling between the tip and the substrate. STM images are therefore sensitive to the detailed atomic structure of the tip, which is largely unknown. This difficulty can be circumvented by adsorbing single atoms or molecules on the tip. Tips functionalized with a known molecular entity are amenable to modeling, allowing theoretical calculations of STM images to reveal the electronic states of the chemisorbed molecule contributing to the tunneling in the STM junction. In addition, the images produced by such tips have an unusually high spatial resolution.[1]

Various schemes have been used to calculate STM images based either on a perturbative Bardeen method or a nonperturbative scattering approach to tunneling, using first-principles or semiempirical methods to describe the electronic structure.[2−7] The Tersoff−Hamann (TH) approximation[2] provides a physically transparent expression for the tunneling current based on the Fermi-level local density of states (LDOS) of the surface in question at the tip apex.[2] The original representation of the tip by an *s* state was later extended by Chen[5] to include other symmetries of the tunneling active tip states. A recent perturbative Bardeen method based on a detailed cluster model of the tip showed that the TH method gave similar results.[8] To apply the TH theory to adsorbates on semiconductors, one must include the electric field produced by the tip; a large bias is needed to obtain STM images for these systems, whereas on metal surfaces, images can be recorded using a small bias and the electric field can be neglected. The general applicability of the perturbative TH method to the calculation of STM images of chemisorbed molecules is not well established, and its usefulness has been questioned.[5] The recent development of calculational schemes based on density-functional theory (DFT) make it possible to assess the TH approximation for chemisorbed molecules on metal surfaces by using electronic states of an electronic structure calculational scheme that also can give a good representation of the chemisorption bond parameters.

There is no consensus opinion about the usefulness of combining the TH approximation and DFT,[9−12] partly because of the limited number of such studies. In calculations of STM images of oxygen on a (111) surface of platinum, Bocquet and Sautet[9] were unable to obtain a good representation of the experimental images, whereas Eichler and co-workers[10] found qualitative agreement between the calculated and experimental images. One shortcoming of both these studies was the short tip−surface distance of about ∼3−4 Å, as the perturbative TH

---

approach is expected to break down in the region of strong tip−surface interaction[2]. Moreover, we recently showed that the experimental STM image of acetylene on the (100) surface of copper could only be reproduced at a large tip−surface distance of about 9 Å.[13] Most recently, a density functional study of STM images for acetylene on Cu(001) and its dehydrogenation products on Cu(001), using cluster models and a localized basis set, were reported by Yuan and co-workers.[14] A qualitative comparison was obtained between simulated images using a TH approach and experimental results.

In this paper, we address the applicability and the utility of the TH approximation for the calculation of STM images of chemisorbed molecules on a metal surface in a combined DFT and STM study of acetylene, ethynyl, and dicarbon chemisorbed on the (001) surface of copper. This sequence of adsorbates is of direct interest in the problem of dehydrogenation and exhibits some interesting trends with respect to their chemisorption properties. The density functional calculations were based on slab models and a plane wave basis set as described in section 2. A key ingredient of the density functional study is the calculation of the bonding geometry, electronic structure, and the vibrational energies of the chemisorbed molecules, and the results are presented in sections 3.1−3.3. In particular, we analyzed the bonding in terms of electronic states derived from molecular orbitals of the chemisorbed molecule. In section 4, we make a direct comparison of the calculated LDOS images presented in section 3.4 with experimental STM images obtained using two qualitatively distinguishable tips.

2. Calculational Method

The electronic structure calculations of the free and chemisorbed C_2H_2, C_2H, and C_2 molecules on a Cu(001) surface were based on density functional theory using the plane-wave, pseudopotential code DACAPO.[15] The exchange-correlation energy was described by the generalized gradient approximation (GGA).[16] The Cu(001) surface was represented by a slab in a super cell geometry. The calculations of STM images required a large surface unit cell with up to 16 atoms.[17] The interactions between the valence electrons and the ion cores were represented by ultrasoft pseudopotentials.[18,19] The geometry was optimized by a quasi-Newton method using Hellmann−Feynman forces.

The electronic structure was investigated by calculating the total density of states (DOS), $\rho(\epsilon)$, for the free molecule and the projected DOSs (PDOSs), $\rho_a(\epsilon)$, on various molecular orbitals of the free molecule with the same geometric structure as the chemisorbed molecule. $\rho(\epsilon)$ was determined in a straightforward manner from the one-electron energies of the Bloch pseudostates for the free molecule. In comparison, the calculation of $\rho_a(\epsilon)$ was not straightforward because we need to calculate overlaps between ultra soft pseudo states, which has been detailed in ref 20. In addition, we had to simulate the continuum of states for a semiinfinite surface by a Gaussian broadening of the discrete spectrum of states in a supercell geometry for each wave vector in the sampling of the SBZ.[21]

We calculated scanning tunneling microscopy (STM) images using the Tersoff−Hamann approach[2]. This approach is based on the Bardeen approximation for the tunneling matrix element and an *s* state representation of the tip electronic structure. In the limit of zero temperature and tip−sample bias, *V*, the differential conductance, d*I*/d*V*, is proportional to the local density of states at the Fermi energy (LDOS), ϵ_F as

$$\frac{\mathrm{d}I}{\mathrm{d}V} = C_0\rho(\boldsymbol{r}_0; \epsilon_F)$$

TABLE 1: Calculated and Experimental Bond Distances and Atomization Energies for the Free C_2H_2, C_2H, and C_2 Molecules

	C_2H_2	C_2H	C_2
d_{CH} (Å)	$1.07(1.06^a)$	$1.07(1.05^c)$	
d_{CC} (Å)	$1.20(1.20^a)$	$1.21(1.22^c)$	$1.28(1.24^e)$
ΔE (eV)	$-17.79(-17.56^b)$	$-11.85(-11.46^d)$	$-6.02(-6.32^e)$

[a] Reference 52. [b] Reference 54. [c] Reference 51. [d] $\Delta E = E_{CC-H} + E_{C-C}$, where E_{CC-H} is from ref 53. [e] Reference 34.

where $\boldsymbol{r}_0$ is the position of the tip apex and the LDOS is defined as

$$\rho(\boldsymbol{r}_0; \epsilon_F) = \sum_{n\mathbf{k}} \mid \psi_{n\mathbf{k}}(\mathbf{r}_0)\mid^2\delta(\epsilon_{n\mathbf{k}} - \epsilon_F) \qquad (1)$$

Here $\psi_{n\mathbf{k}}(\mathbf{r})$ is a Bloch wave function of the chemisorbed molecule with band-index n, wave vector $\mathbf{k}$ in the SBZ and energy $\epsilon_{n\mathbf{k}}$ and ϵ_F is the Fermi energy.[22] The continuum of states of a semiinfinite surface was simulated in the same manner as for the PDOS. The proportionality constant C_0 is given by[25]

$$C_0 = 8\pi^3\frac{e^2\hbar^3}{m^2} R^2 \exp(2\kappa R)\rho_s(\epsilon) \qquad (2)$$

where R is the effective radius of curvature, κ is the decay constant of the *s* state in the vacuum region and $\rho_s(\epsilon_F)$ is the projected DOS of tip states on the *s* state.

We calculated the vibrational energies and modes of the free and chemisorbed acetylene and ethynyl molecule within the harmonic approximation by diagonalizing the dynamical matrix.[26] A row of the dynamical matrix is determined from the differential changes of the forces acting on the ion-cores when making an displacement of an ion core. These differential changes were approximated by central differences by calculating Hellmann−Feynman forces for finite displacements of about 0.05 Å. The substrate is treated as being rigid; that is, the substrate atoms are kept at their equilibrium positions, so that the number of degrees of freedom is determined by the number of atoms in the molecule.

3. Results and Discussion

3.1. Bonding Geometry and Energies. Before presenting our results for bonding geometries and energies for the chemisorbed molecule, we first show that our DFT calculations gives a good description of these properties for the free molecules and the free surface.

The structure of the bare surface was optimized by allowing the two uppermost layers to relax in all directions and by fixing the two lowermost layers at the bulk positions with the calculated bulk lattice parameter $a = 3.65$ Å. The calculated relative changes in layer distances between the first and second layer, $\Delta d_{12} = -1.98\%$, and between the second and third, $\Delta d_{23} = +1.6\%$, from the bulk interlayer distance are in good agreement with low energy electron diffraction data:[27] $\Delta d_{12} = -1.1 \pm 0.4\%$ and $\Delta d_{23} = +1.7 \pm 0.6\%$.

We find that the calculated equilibrium configurations and energetics of the free molecules are in good agreement with experiments and the density functional study by Yuan and co-workers.[14] The linear configuration, the calculated interatomic distances, and the atomization energies for the molecules are in good agreement with experimental data as shown in Table 1. The atomization energies show directly that C_2 and C_2H have a large hydrogen affinity. The corresponding energy differences give directly the binding energy of an H atoms with the
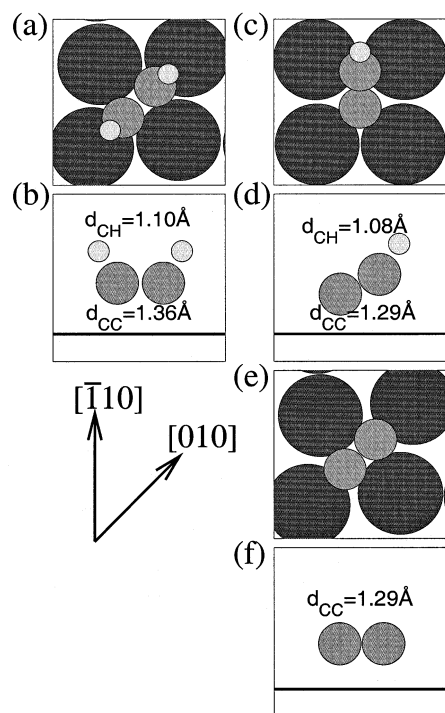
Figure 1. Calculated equilibrium configurations of C_2H_2, C_2H, and C_2 chemisorbed on Cu(001). Parts a, c, and e are top views of C_2H_2, C_2H, and C_2, respectively, whereas parts b, d, and f are the corresponding side views. Four Cu atoms in the top layer and the C and H atoms are represented by large, medium, and small circles, respectively. The C−C and C−H bond lengths are indicated. The results were obtained using a 4 layer, 3×3 Cu slab.

molecules: 5.94 and 5.83 eV for C_2H and C_2, respectively. Although C_2 readily accepts a H for H_2S or H_2O to from C_2H, the lack of observation of similar H transfer to C_2H, forming C_2H_2, may be due to the rotational motion of C_2H which leads to steric hindrance to the reaction[28]

To determine the equilibrium configuration of the chemisorbed molecules on Cu(001), we have considered two possible orientations of the C−C axis, being either along the $[\bar{1}10]$ direction or the [010] direction. For both orientations, the geometries were optimized in such a way that the molecules were allowed to relax in the plane spanned by the surface normal and the C−C axis, and all Cu atoms in the two topmost layers of the surface were allowed to relax in all directions. As shown in Figure 1, the equilibrium configuration of the C−C axis is along the [110] direction for the C_2H molecule and has a C_s adsorption site symmetry, whereas the equilibrium configurations of C_2H_2 and C_2 have both the C−C axes along the [010] direction and have a C_{2v} adsorption site symmetry.

The chemisorbed C_2H_2 and C_2H molecules have different geometric structure than that for the free molecules as shown in Figure 1. The chemisorbed C_2H molecule is bent with a C−C−H bond angle of 150°, the C−C axis is tilted 63° relative to the surface normal, and the C−C bond length (d_{CC}) is increased by 0.07 Å from its value of the free molecule, whereas the C−H bond length (d_{CH}) increases only 0.01 Å. Also the chemisorbed C_2H_2 molecule is bent, the C−C−H bond angles are 120°, but the C−C axis is parallel to the surface. In this case, the d_{CH} and d_{CC} are increased by 0.03 and 0.16 Å from their gas-phase value, respectively. This dramatic elongation of the C−C bond to 1.37 Å is in agreement with the value of 1.42 ± 0.05 Å suggested by surface extended X-ray absorption fine structure (SEXAFS) measurements.[29] The C−C axis of the chemisorbed C_2 molecule is parallel to the surface, and d_{CC} is
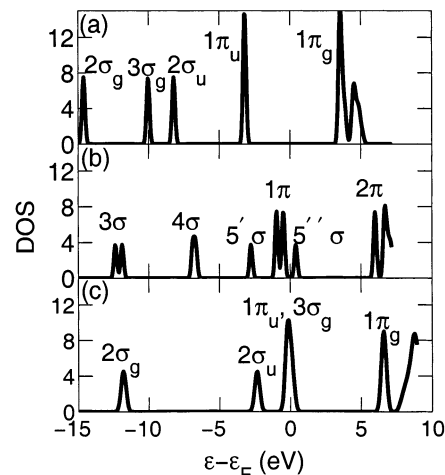
Figure 2. Calculated density of states (DOS) for the free, linear C_2H molecule. The character of the molecular states has been indicated using the symmetry labels for C_∞. Note that the groundstate of C_2H is spin polarized and that the $1\pi_u$ and $3\sigma_g$ orbitals are nearly degenerate.

increased by less than 0.01 Å. The relaxations of the substrate atoms induced by the chemisorbed molecule are substantial. This effect is largest for the chemisorbed C_2 and smallest for the chemisorbed C_2H_2.

The calculated chemisorption energies show a strong variation for this sequence of molecules on Cu(001). The calculated binding energies (excluding zero-point energies) are 1.31, 4.22, and 6.57 eV for C_2H_2, C_2H, and C_2, respectively. This large variation of the binding energies is not unexpected in view of the electronic structure of the free molecules, as discussed in section 3.2. The large calculated binding energy of 2.39 eV for H on Cu(001)[30] and the large increase in binding energies with decreasing number of H atoms bonded to C_2 result in a dramatic lowering of the affinities of a chemisorbed H atom for C_2H and C_2 of 0.54 and 1.09 eV, respectively, from the affinity of about 6 eV in the gas phase.

The energy difference between the two orientations considered for the chemisorbed molecules may be viewed as an energy barrier for rotations of the molecule among the equivalent minimum energy orientations of the molecule. This energy barrier is only about 85 and 75 meV for C_2H_2 and C_2H, respectively, whereas it is much larger, 315 meV, for C_2. The trends of these results are in agreement with the corresponding experimental values of 169 and 56 meV for C_2H_2[31] and C_2H,[32] respectively. The experimental values were obtained by a fit of measured rotation rates as a function of substrate temparature to an Arrhenius expression.[32]

3.2. Electronic Structure. To gain an understanding of the electronic structure of the chemisorbed C_2H_2, C_2H, and C_2 molecules, we have also studied the electronic structure of the free molecules both in linear and bent configurations.

The bonding of C_2H in terms of MOs can be understood from the classical bonding models of a homonuclear, diatomic molecule such as C_2 and sp hybridization for C_2H_2.[33] In Figure 2, we present calculated density of states (DOS) for the free C_2H_2, C_2H, and C_2 molecules that show directly the occupancies and energies of the molecular orbitals (MOs). These DOS show that the bonding of a single H atom to C_2 results in a triple C−C bond with a similar bond distance as the triple bond C_2H_2. The double bond of C_2 results in a longer bond distance, see Table 1.[35] The 4σ orbital is a bonding combination of the H 1s AO with a C sp AO and is essentially nonbonding with respect to the C−C interaction, whereas the 3σ MO is bonding and

**8164** *J. Phys. Chem. B, Vol. 106, No. 33, 2002*

Olsson et al.
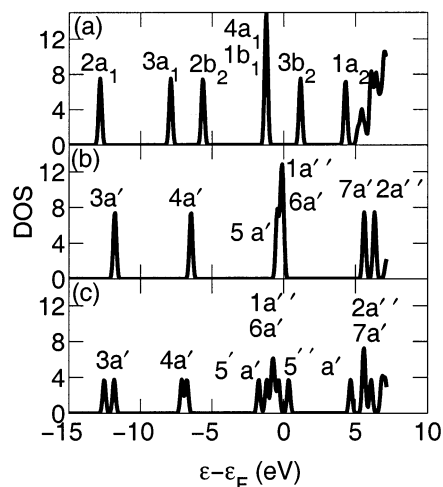
Figure 3. Calculated density of states (DOS) for the free, bent molecules: (a) C_2H_2, (b) C_2H (spin unpolarized), and (c) C_2H (spin polarized). The geometric configurations are the same as in Figure 1b,d for C_2H_2 and C_2H, respectively. The character of the molecular states has been indicated using the symmetry labels of C_{2v} and C_s. Note that $1a''$ and $6'$ are nearly degenerate. The two spin split states of $5a'$ are labeled $5'a'$ and $5''a'$, respectively.

correlates with the $2\sigma_g$ MO of C_2H_2. The remaining sp orbital forms a dangling bond that is split into a singly occupied $5'\sigma$ orbital, an unpaired electron in the 1π orbital, and a single unoccupied $5''\sigma$ orbital. As shown in Figure 2, the strong spin-polarization of the 5σ orbital induces also a weak spin splitting of 1π, 2π, and 3σ orbitals through the C−C bond.

Because the chemisorbed C_2H_2 and C_2H molecules have a bent geometric configuration, as described in section 3.1, we have investigated the effect of the bending of the free, linear molecules on the electronic structure. The intramolecular distances and angles of the free bent molecule in the yz plane are chosen to be the same as for the chemisorbed molecule (see Figure 1). The bending of the molecules lowers the C_∞ symmetry to a C_{2v} symmetry with symmetry characters a_1, a_2, b_1, and b_2, and to a C_s symmetry with symmetry characters a' and a'' for the C_2H_2 and the C_2H molecules, respectively. The resulting labeling of the molecular orbitals of the bent molecules are shown by the calculated DOS in Figure 3. The low-lying $2a_1$ of C_2H_2 and $3a'$ of C_2H derive from $2\sigma_g$ of the linear C_2H_2 and 3σ of the linear C_2H, respectively.

The effect of the bending of C_2H_2 on the frontier orbitals has been nicely discussed by Hoffmann and co-workers[36,37] using extended Hückel calculations, and their picture is supported by our calculations. The C in-plane p AOs hybridize with the C s AOs and forms sp^2 orbitals at a bending angle of 60°. Two of these sp^2 orbitals contribute to the symmetric, $3a_1$, and antisymmetric, $2b_2$, combinations of C−H bonding MOs, whereas the remaining sp^2 AOs form the C−C bonding, $4a_1$, and antibonding, $3b_2$, combinations. The C out-of plane p AOs are mainly unaffected and form the C−C bonding, $1b_1$, and antibonding, $1a_2$, MOs. The effect of the bending on the MOs of the linear C_2H is similar as shown by the DOS in Figure 3, but the effect is smaller because the bending angle is only about 30° and no genuine sp^2 orbitals are formed. The π MOs, $1a''$ and $2a''$, of C_2H are very similar in character to the $1b_1$ and $1a_2$ orbitals of C_2H_2, and the $6a'$ and $7a'$ are analogous to the $4a_1$ and $3b_2$ orbitals of C_2H_2, respectively.

The electronic structure of the chemisorbed C_2H_2, C_2H, and C_2 molecules on Cu(001) have been characterized from the DOS projected on the (spin-unpolarized) MOs of the free bent C_2H_2 and C_2H, and the free C_2. As shown in Figures 4a, 5a, and 6a,
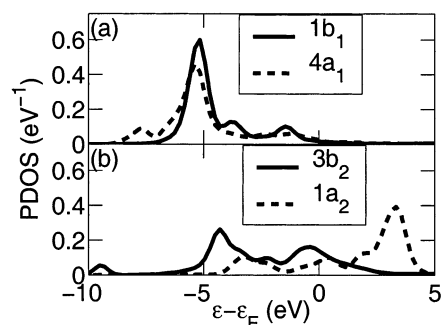
Figure 4. Calculated projected density of states (PDOS) of C_2H_2 chemisorbed on Cu(001). The DOS are projected on (a) the bonding and (b) the antibonding molecular orbitals in Figure 3a for the bent C_2H_2 molecule.
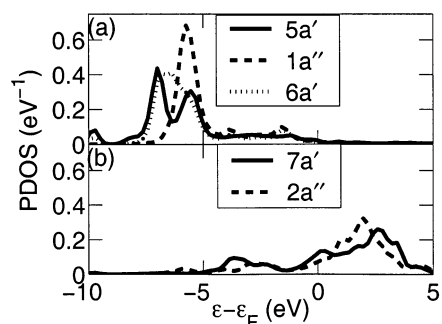

Figure 5. Calculated projected density of states (PDOS) of C_2H chemisorbed on Cu(001). The DOS are projected on (a) the bonding and (b) the antibonding (spin-unpolarized) molecular orbitals in Figure 3b for the bent C_2H molecule.
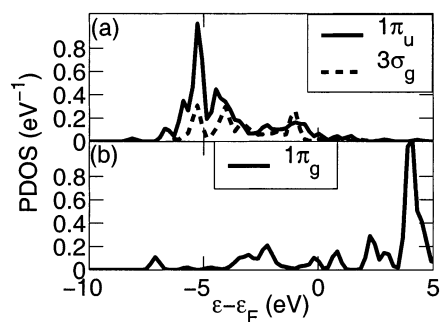
Figure 6. Calculated projected density of states (PDOS) of C_2 chemisorbed on Cu(001). The DOS are projected on (a) the bonding and (b) the antibonding molecular orbitals in Figure 2c for the free C_2 molecule.

the $1\pi_u$ MOs of C_2 and the related $1a''$ and $6a'$ MOs of C_2H and $1b_1$ and $4a_1$ MOs of C_2H_2 interact strongly with the d-band of Cu in the energy range of −5 to −2 eV and are more or less shifted below the d-band. The singly occupied $5a'$ orbital of C_2H and the unoccupied $3\sigma_g$ of C_2 become doubly occupied, resulting in a strong surface chemical bond and no spin polarization of the chemisorbed C_2H. The PDOS in Figures 4b, 5b, and 6b show that the antibonding $1\pi_g$ MOs of C_2, the related $7a'$ and $2a''$ MOs of C_2H, and the $3b_2$ and $1a_2$ MOs of C_2H_2 are all appreciably broadened by their interaction with substrate states and acquire a substantial fractional occupation for C_2H_2 and C_2H. In particular, this occupation is larger for C_2H_2 than C_2H as reflected by the larger bond elongation for C_2H_2 than for C_2H.

The electron transfer to unoccupied MOs of C_2H_2, C_2H, and C_2 upon chemisorption show up in the difference between the electron density of the chemisorbed molecule and the sum of the electron densities of the isolated molecule and the bare

C$_2$H$_2$, C$_2$H, and C$_2$ on Cu(001)

J. Phys. Chem. B, Vol. 106, No. 33, 2002 **8165**
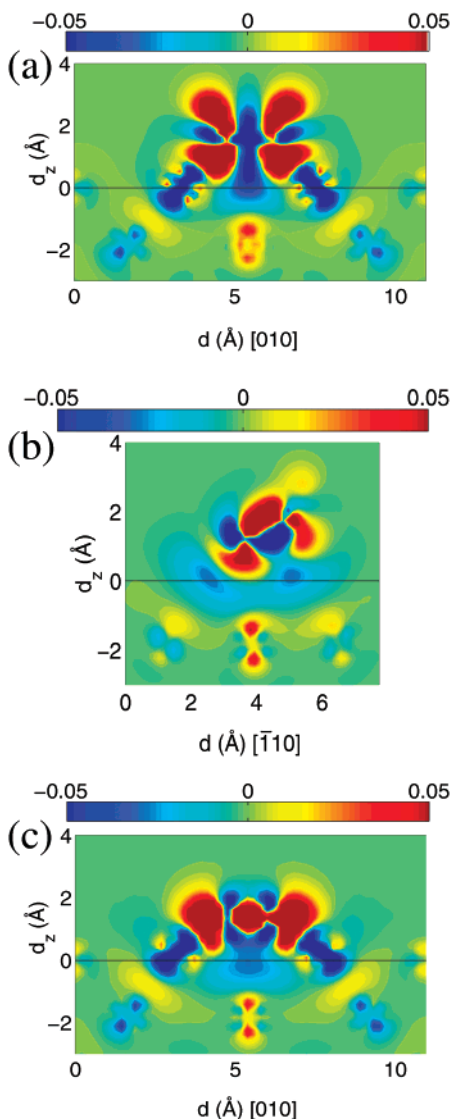
Figure 7. Density difference contours along the C−C axes of (a) C$_2$H$_2$, (b) C$_2$H, and (c) C$_2$. Density differences for values larger than 0.05 and less than −0.05 electrons/Å^3 are truncated. $d_z = 0$ corresponds the position of the surface layer. The calculation has been carried out in a 3×3 surface unit cell with 16 k points in the SBZ.

TABLE 2: Calculated and Experimental Vibrational Energies for Various Stretch Modes of C$_2$H$_2$ on Cu(100)^a

	$\hbar\omega$ (meV)	
mode	theory	expt
H−CC−H (D-CC-D) (ss)	379 (281)	
H−CC−H (D-CC-D) (as)	375 (275)	357^a (265^a)
DCC−H (HCC-D)	377 (278)	360^a (269^a)
HC−CH	171	164^b

^{a} (ss) and (as) refer to the symmetric and antisymmetric stretch modes, respectively. ^{b} IETS data from ref 45. ^{c} EELS data from ref 41.

both from localized d and extended sp metal states. Also, the screening of the charge transfer into the MOs by the conduction electrons contributes to the extended regions of charge depletion. These regions are very similar to the regions appearing in the results for electronegative adsorbates such as Cl, S, and O on jellium surfaces.[38,39]

3.3. Vibrational Modes. The vibrational energies and modes of chemisorbed molecules are characteristic signatures of their identity and provide some information about the nature of the chemisorption bond. Here, we will primarily present and discuss our results for some selected sets of modes of the free and chemisorbed C$_2$H$_2$, C$_2$H, and C$_2$. Our calculated vibrational energies are in agreement with the results of Yuan and co-workers.[14]

The vibrational modes of the chemisorbed molecules that derive from internal modes of the free molecule have typically large energies compared to the substrate phonon energies and should be well-described in the rigid substrate approximation. The calculated energies of the C−C stretch modes of the chemisorbed C$_2$H and C$_2$H$_2$ molecules are 204 and 171 meV, respectively. These energies show appreciable downward shifts of 53 and 68 meV from the energies of the free, linear C$_2$H and C$_2$H$_2$ molecules, respectively. As shown in section 3.2, these large downward energy shifts are consistent with the filling of C−C antibonding MOs upon chemisorption. The energies of the C−H stretch modes decrease also upon chemisorption. The average value of 399 meV for the symmetric and antisymmetric stretch mode energies for the free C$_2$H$_2$ molecule and their splitting of 10 meV, Table 2, decreases to 377 and 4 meV, respectively, upon chemisorption. For the C−H stretch mode of the C$_2$H molecule, the corresponding downward shift of 19 meV is similar in magnitude. The symmetric and antisymmetric in-plane C−H bending modes for the chemisorbed C$_2$H$_2$ molecule have larger energies, 117 and 132 meV, than the energy of 79 meV for the in-plane C−H bending mode of chemisorbed C$_2$H molecule.

The remaining vibrational modes of the chemisorbed molecule derive essentially from frustrated rotations and translations of the free molecules. The frustrated rotational modes are given by the C−H out-of-plane bending mode with energy 74 meV for C$_2$H and the antisymmetric one with energy 101 meV for C$_2$H$_2$. We find that the remaining modes except the frustrated cartwheel mode of C$_2$H$_2$ at 75 meV have vibrational energies close to the bulk phonon band, which has a maximum phonon energy of 30 meV.

Our calculated vibrational energies for the stretch modes of the free linear molecules are in relatively good agreement with experimental data. The calculated energies of the C−C stretch modes of C$_2$H$_2$ are 239 meV, in good agreement with the experimental value of 245 meV, whereas the C−C stretch energy of C$_2$H, 257 meV, is larger than the experimental value of 229 meV.[40] The calculated average energy of 399 meV for the symmetric and antisymmetric C−H stretch modes of C$_2$H$_2$

surface. The contours of such density difference in the plane spanned by the C−C axis and the surface normal are presented in Figure 7, for all of the molecules. A common feature is the large enhancement of the electron density at the molecule with a shape that is specific for each molecule. In the case of the chemisorbed C$_2$H$_2$, the shape can be understood from the partial filling of the $3b_2$ MO. For C$_2$H, the filling of the $5a'$ MO gives a large contribution, but the lobe extending into the vacuum region is derived from the $7a'$ MO. In the case of C$_2$, the situation is less clear. The structure in the C−C bonding region is derived from the filling of the $3\sigma_g$ MO, and the two small outer lobes are derived from the partial filling of the antibonding $1\pi_g^\perp$ MO of the 2-fold degenerate $1\pi_g$ MOs. The lobes of $1\pi_g^\perp$ MO are oriented perpendicular to the surface. The nodal plane of this MO is obstructed by the density associated with the $3\sigma_g$ MO. Note that the $1a_2$, $2a''$, and $1\pi_g^\parallel$ MOs, whose lobes are parallel to the surface, for the C$_2$H$_2$, C$_2$H, and C$_2$ molecules, respectively, have a node at the molecular plane, and the partial filling of these MOs does not contribute to the presented density difference contours. As also shown by the density difference contours, the electron transfer to the unoccupied MOs are taken

TABLE 3: Calculated and Experimental Vibrational Energies for Various Stretch and Bending Modes of C$_2$H on Cu(100)

|	$\hbar\omega$ (meV)	
mode	theory	expt
CC−H (CC-D) stretch	410 (307)	395,[a] 374[b] (313)[a]
C−CH stretch	204	179[b]
in-plane CC−H (CC-D) bend	79 (61)	81[a] (62)[a]
out-of-plane CC−H bend	74 (55)	

[a] IETS data from ref 45. [b] EELS data from ref 41.

and the energy of 429 meV for the C−H stretch mode of C$_2$H are in good agreement with the corresponding experimental values of 413 and 447 meV.[40] In particular, the calculated splitting of 10 meV between the symmetric and antisymmetric mode is in excellent agreement with the experimental value of 9.5 meV.

In Tables 2 and 3, we make a direct comparison of our calculated mode energies with available experimental data for the chemisorbed molecules. The overall agreement between calculated and experimental values is typically within 5%, except for the electron-energy-loss data (EELS) for C$_2$H.[41] In these EELS measurements, the identity of the molecules produced by thermal decomposition of C$_2$H$_2$ was never unambiguously determined and was even attributed to CCH$_2$ species. Recently, the density functional study by Yuan and co-workers[14] showed that the calculated vibrational energies of the CCH$_2$ species supported the formation of CCH$_2$ species.

The C−H stretching modes provides an interesting class of modes for comparison of theory with experiments. Recent vibrational inelastic electron tunneling (IET) measurements on acetylene and its deuterated species[42] show that the detected C−H and C−D stretch modes of C$_2$H$_2$ and C$_2$D$_2$ are 2 and 3 meV below the energies of the C−H and C−D stretch modes for the C$_2$HD isotope, in excellent agreement with the calculated values shown in Table 2. The larger splitting between the symmetric and antisymmetric modes for the C−D stretch modes than for the C−H stretch modes is counterintuitive considering a simple argument based on the scaling of the vibrational energy on the mass of the H and D atoms, which gives that the splitting between the symmetric and antisymmetric combinations should be a factor of $(2)^{1/2}$ smaller for the C−D than the C−H stretch mode. The anomalous isotope behavior of the splitting is caused by the larger participation of the motion of the C atoms in the C−D stretch modes than for the C−H modes resulting in a larger indirect coupling mediated by the C atoms between the motion of the D atoms than for the motion of the H atoms. An anomalous isotope effect is also present in the upward energy shift from the antisymmetric C−H stretch mode of the chemisorbed C$_2$H$_2$ to the C−H stretch mode of the chemisorbed C$_2$H. The observed shifts are 38 and 48 meV for the C−H and the C−D stretch modes, respectively.

The assignment of the observed C−H bending modes by EELS[41] and IETS[32] is less clear. In the EELS data from C$_2$H$_2$ on Cu(001), the observed losses at 141, 118, and 78 meV were attributed to C−H bending modes, which are consistent with the calculated energies 132 and 117 meV of the antisymmetric and symmetric in-plane bending modes, respectively, and 101 and 75 meV for the antisymmetric and symmetric out-of-plane bending modes, respectively. For the chemisorbed C$_2$H, the calculated energies of the in-plane and out-of-plane bending modes are relatively close in energy so that an assignment of the observed peak in the IETS peak at 81 meV based on energies only is ambiguous considering the accuracy of the calculated
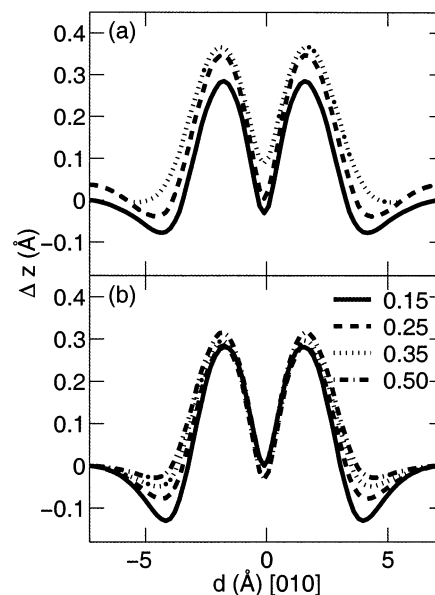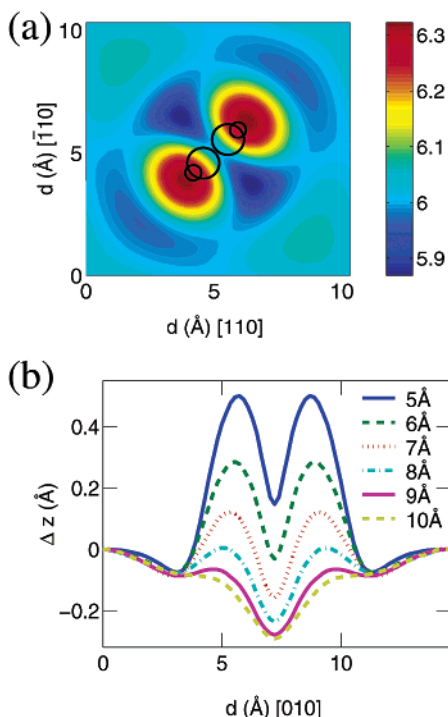

Figure 8. Calculated LDOS profiles, Δz, along the C−C axis of C$_2$H$_2$ chemisorbed on Cu(001). (a) Different supercell sizes and k-point sets in the SBZ. Dashed and solid lines are profiles for 4 × 4 surface unit cells using 9 and 16 points in SBZ, respectively, and the short-dashed line is the profile for the 3 × 3 surface unit cell using 16 points in the SBZ. All profiles are for the same value of $\rho(\mathbf{r}, \epsilon_F)$. (b) Different Gaussian broadenings, $\sigma = 0.15$−0.50 eV, of energy levels. $\Delta z = 0$ corresponds to a tip−surface distance of 6 Å in both a and b. Note that the center of the C$_2$H$_2$ molecule is at (a) $d_{[010]} = 0$ Å and (b) $d_{[010]} = 7.3$ Å.

vibrational energies and the experimental uncertainties in determining vibrational energies.

3.4. STM Images. In this section, we present calculated STM images of C$_2$H$_2$, C$_2$H, and C$_2$ chemisorbed on Cu(001) using the Tersoff−Hamann approach and discuss these images in relation to the adsorbate-induced electronic structure. The calculated images are contours of tip−surface distances, $\mathbf{r}$, over the surface at constant local density of states, $\rho(\mathbf{r}, \epsilon_F)$, at the Fermi energy. These topographical images of the LDOS and their profiles along various directions in the surface unit cell are henceforth referred to as LDOS images and profiles. Before discussing the calculated images we show (1) that the surface unit cell is sufficiently large to represent an isolated molecule, (2) that the results are well converged with respect to k-point sampling of the surface Brillouin zone (SBZ), and (3) that the results are rather insensitive to the energy broadening used to simulate the continuum set of states for a semiinfinite surface.

Because we want to model STM images of isolated molecules on a surface, we need to investigate the effect of the surface unit cell size on the LDOS image. In Figure 8a, we present LDOS images of C$_2$H$_2$ chemisorbed on Cu(001) in both 3 × 3 and 4 × 4 surface unit cells. The protrusions in the calculated LDOS profile along the molecular axis for the 3 × 3 surface unit cell cover a large fraction of the cell, which indicate that this cell might be too small. As shown in Figure 8a, the LDOS profiles in 3 × 3 and 4 × 4 surface unit cells with the same k-point density in the SBZ, 16 and 9 k points, respectively, only show small differences in their common region, and the protrusions are well-contained in the larger cell. Hence, the 4 × 4 surface unit cell is large enough to represent an isolated C$_2$H$_2$ molecule, and even the 3 × 3 surface unit cell is acceptable in this respect. In the following, all results are based on 4 × 4 surface unit cells.

To check the convergence of the calculated LDOS images with respect to the number of k points in SBZ, we have

Figure 9. Calculated LDOS (a) image and (b) profiles along the C−C axis for C$_2$H$_2$ chemisorbed on Cu(001), where $\Delta z = 0$ corresponds to tip−surface distances of $z_0 = 5, 6, 7, 8, 9,$ and 10 Å, (a) $z_0 = 6$ Å. The geometric configuration of the chemisorbed C$_2$H$_2$ is indicated in the LDOS image. The calculation was carried out using a 4×4 surface unit cell with 16 points in the SBZ and Gaussian broadening of $\sigma = 0.25$ eV.[21]
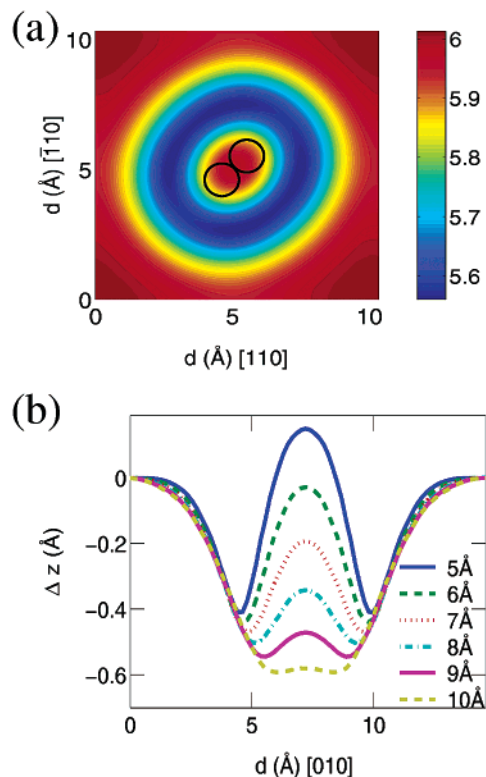
calculated LDOS images for chemisorbed C$_2$H$_2$ using 9 and 16 k points. As shown in Figure 8a, the profiles almost fall on top of each other. Hence, the calculated LDOS profiles are well converged with respect to k-point sampling. In the following, all results are based on 16 points in SBZ.

As discussed in section 2, we introduce an energy broadening, σ, of the δ functions in order to model a semiinfinite system with a finite slab. This broadening should be chosen in such a way that there is only a small change in the images for different values of σ. In Figure 8b, we present LDOS profiles along the C−C axis of chemisorbed C$_2$H$_2$ with 0.15 eV $\leq \sigma \leq$ 0.50 eV. The LDOS profiles with 0.25 eV $\leq \sigma \leq$ 0.50 eV show only small differences, whereas the LDOS profile with $\sigma = 0.15$ eV deviates somewhat from the other profiles. An indication that $\sigma = 0.15$ eV may be too small to properly represent the set of continuum states is the fact that we have on average about 8 electronic states/eV for each k point. We conclude that 0.25 eV $\leq \sigma \leq$ 0.50 eV is an acceptable range for σ. In the following, all results are based on $\sigma = 0.25$ eV.

The LDOS images and profiles of chemisorbed C$_2$H$_2$, C$_2$H, and C$_2$ on Cu(001), shown in Figures 9, 10, and 11 respectively, show similar topographical features, such as one large depression and one or two protrusions. The LDOS images show that these features are large compared to the size of the molecule. Furthermore, the protrusions show some interesting dependencies with tip−surface distance. We present several evidences that the protrusions in the LDOS images for C$_2$H$_2$ and C$_2$H derive from molecular states overlapping with states at the Fermi energy and that the depressions are associated with two effects: (1) the screening of electron charge transferred to the molecule by the free-electron like Cu states and (2) electron transfer from the latter states into states derived from MOs. These evidences are based on an analysis using the symmetries
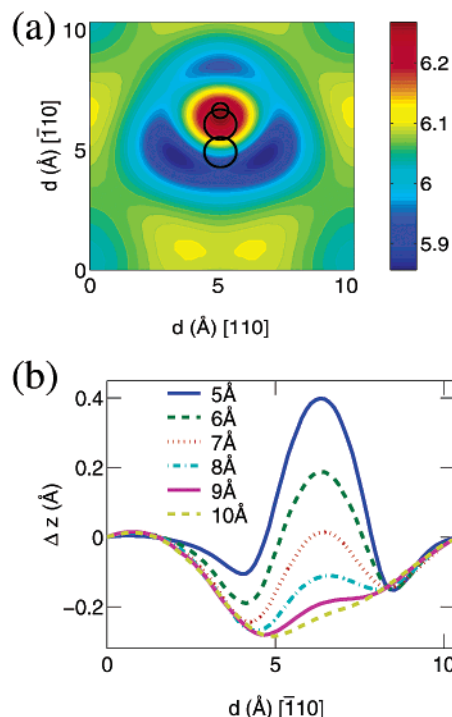
Figure 10. Calculated LDOS (a) image and (b) profiles along the C−C axis for C$_2$H chemisorbed on Cu(001), where $\Delta z = 0$ corresponds to tip−surface distances of $z_0 = 5, 6, 7, 8, 9,$ and 10 Å, (a) $z_0 = 6$ Å. The geometric configuration of the chemisorbed C$_2$H is indicated in the LDOS image. Same surface unit cell, k-point set, and σ as in Figure 9.

Figure 11. Calculated LDOS (a) image and (b) profiles along the C−C axis for C$_2$ chemisorbed on Cu(001), where $\Delta z = 0$ corresponds to tip−surface distances of $z_0 = 5, 6, 7, 8, 9,$ and 10 Å, (a) $z_0 = 6$ Å. The geometric configuration of the chemisorbed C$_2$ is indicated in the LDOS image. Same surface unit cell, k-point set, and σ as in Figure 9.

of the MOs, density differences, and dependencies on LDOS profiles with tip−surface distances.

For C_2H_2 on Cu(001), the two protrusions in the LDOS image and profiles, Figure 9a,b derive from the $3b_2$ MO. The $3b_2$ MO gives a large contribution to PDOS at ϵ_F and is symmetric (antisymmetric) with respect to a plane along (perpendicular to) the molecular axis, which explains the nodal plane in the LDOS image. The other MO with a large contribution to PDOS at ϵ_F, $3a_2$, is antisymmetric both with respect to a plane perpendicular to and along the molecular axis, which would give rise to two nodal planes in the LDOS image. Thus, the $3a_2$ MO does not give a large contribution to the protrusions in the LDOS images. Moreover, wave functions at ϵ_F that overlap with the $1a_2$ MO decay faster in the vacuum regions than the $3b_2$ MO because the former wave function has a larger lateral distribution and lateral kinetic energy in this region than the latter wave function. The same kind of argument about the decay of the wave functions perpendicular to the surface explains the decrease of the protrusions relative to the background with increasing tip−surface distance in the LDOS profiles, Figure 9b.

A corroboration of the interpretation that the protrusions in the LDOS image of C_2H_2 derive from the $3b_2$ MO is the change of the separation between the two protrusions with the tip−surface distance z_0 at the boundary of the surface unit cell. At $z_0 = 5$ Å, the distance between the two protrusions is 3.0 Å, whereas it increases to 5.0 Å at $z_0 = 9$ Å. This increase can be explained by the spatial extension of the wave functions contributing to the image. In the density difference contours along the C−C axis of C_2H_2, Figure 7c, the density difference increase is associated with the $3b_2$ MO being almost completely filled on the surface. Because the outer lobes of the $3b_2$ MO are tilted with respect to the surface normal, its wave function will expand in that direction and shift the positions of of the two protrusions.

The single protrusion in the LDOS image and profiles of C_2H chemisorbed on Cu(001), Figure 10a,b, is derived from the MO, $7a'$, and can be explained similarly as the protrusions in the LDOS images of C_2H_2. The $7a'$ MO has a large contribution to PDOS at ϵ_F, extends away from the surface, and has the correct symmetry with no nodal planes. The other MO that has a large overlap with electron states at ϵ_F, $2a''$, is antisymmetric with respect to the molecular axis, and its contribution to the LDOS is expected to be suppressed. The $2a''$ MO has no lobe on the H atom and has a larger lateral spatial variation than the $5a'$ MO, which results in a faster decay away from the surface for states that derive from $2a''$ MO than for the $5a'$ MO.

The position of the protrusion in the LDOS image of C_2H shifts somewhat with increasing tip−surface distances, which is explained by the spatial extension of the $7a'$ MO in a similar manner as for the C_2H_2 images discussed earlier. The position of the protrusion shifts 0.3 Å away from the center of the C_2H molecule when z_0 increases from 5 to 9 Å. However, because the lobe of the $7a'$ MO has a smaller tilt angle with respect to the surface normal than the $3b_2$ MO of C_2H_2, its wave front will extend closer to the surface normal and the shift will be smaller.

The LDOS image of chemisorbed C_2, Figure 11a, has one protrusion in the center of the molecule, but its origin is less clear than for the protrusions of the LDOS images for C_2H_2 and C_2H. In this case, we have no pronounced contributions from any MOs of C_2 to the PDOS at ϵ_F. However, the symmetry of the protrusion is consistent with the symmetry of the $3\sigma_g$ and $1\pi_u^\perp$ MOs. Because the $1\pi_u^\perp$ MO extends into the vacuum region whereas for $3\sigma_g$ it extends along the surface, we suggest that the $1\pi_u^\perp$ MO gives the main contribution to the LDOS.

In contrast to the protrusions in the LDOS images that derive from molecular states of the adsorbate, we argue that the depressions in the LDOS images are associated with adsorbate-induced effects on the free-electron like metal states dominating $\rho(\boldsymbol{r},\epsilon_F)$ of the bare Cu, as suggested by STM calculations for other electronegative species.[43,44] This argument is based on the following two indications.

The first indication is the density difference decrease of chemisorbed C_2H_2, C_2H and C_2, shown in Figure 7. The spatial extension of the depression is about as large as the extension of the electron depletion in the density difference contours displayed in Figure 7a−c, for all three adsorbates. Furthermore, as can be seen from the PDOSs for the adsorbed C_2H_2, C_2H, and C_2 in Figures 4−6, respectively, the chemisorption involves electron transfer from the surface to the adsorbate, but no significant redistribution of electrons among the MOs. The decrease of the free-electron-like density around the molecule has two contributions: (1) screening of the transferred electron charge into the molecular states by the free-electron like states and (2) charge transfer from the free-electron like states to the molecular states. Both of these effects involve all occupied free-electron-like states, including the ones at ϵ_F, and should affect $\rho(\boldsymbol{r},\epsilon_F)$ in the remote tip region.

The second indication is that the shapes of the depressions are very similar for different z_0. This behavior can be seen in the LDOS profiles along the molecular axes of C_2, Figure 11b, and C_2H for $z_0 \geq 6$ Å, Figure 10b. The more pronounced depressions with increasing z_0 are due to the faster decrease of the electronic states contributing to the protrusions than for the free-electron like states, as discussed earlier.

Finally, the simulated STM images by Yuan and co-workers[14] show some similarities with our results. However, we cannot make a direct comparison of the results because they do not provide the signs or the magnitudes of their calculated isoheights of partial density of states, or the tip−surface distances.

4. Comparison with Experiments

In this section, we compare the calculated LDOS profiles with the measured constant-current STM profiles for C_2H_2, C_2H, and C_2 chemisorbed on Cu(001) for two different tips that produce distinct types of images. In general, a direct quantitative comparison between calculated and measured images is precluded by uncertainties in the tip structure, composition, and distance from the surface. The primary objective of this comparison is to see whether the calculated LDOS images can reproduce the observed STM images for this set of molecules at reasonable tip−surface distances. We also compare measured tunneling resistances with estimates based on the simple tip model introduced by Stokbro and co-workers.[25]

The experimental profiles shown in Figure 12 were acquired with what will be referred to as a "sharp" tip. Especially notable are the significant protrusions seen in profiles of each species that are not as pronounced, or even evident, in previously published images with a "typical" tip. The tip was produced by the electron-induced dissociation of H_2S species adsorbed on a tungsten tip while in tunneling range of the surface. Unlike ref 1, the adsorbed species at the tip end could not be unambiguously identified because these species could not be reversibly transferred between the surface and the tip. The facile dissociation of the surface adsorbed H_2S, however, suggests that atomic S is produced at the end of the tip under appropriate conditions. We expect that the bonding of a S atom to the metallic tip to involve mainly p orbitals of S and that tunneling should be dominated through a single p_z orbital. We have found, however,
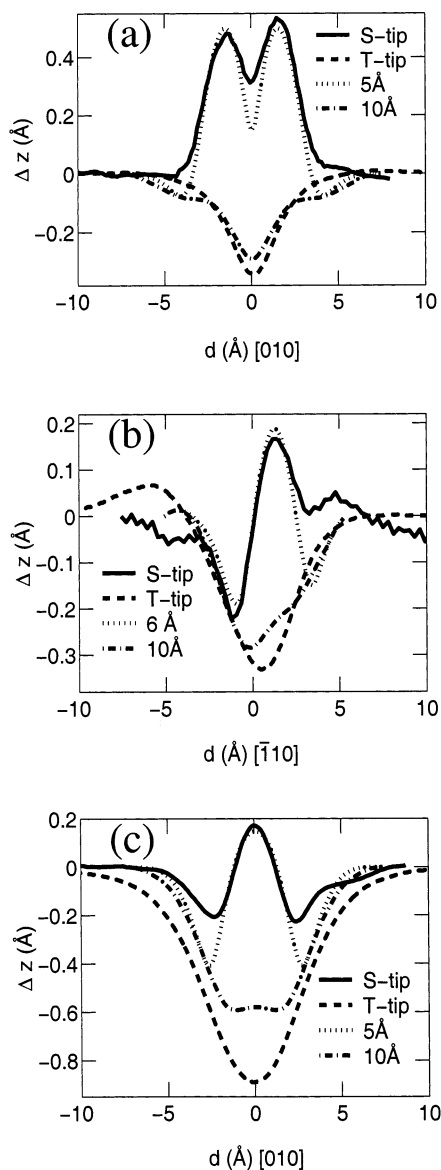
Figure 12. Comparison of experimental and theoretical profiles for C$_2$H$_2$, C$_2$H, and C$_2$ on Cu(001). The experimental profiles are obtained with a "sharp" or a "typical" tip, as indicated by S tip and T tip, respectively. The theoretical profiles, dotted lines, are the same as presented in Figures 9b, 10b, and 11b at indicated tip–surface distances. The experimental tunneling conditions for the "typical" tip profiles were 10 pA and 50 mV, and for the "sharp" tip profiles of C$_2$H$_2$, C$_2$H, and C$_2$, the tunneling conditions were 1 nA and 250 mV, 10 pA and 50 mV, and 1 nA and 50 mV, respectively.

that the LDOS images based on a "sharp" tip representation with a p$_z$ orbital has a more or less identical shape and corrugation for the LDOS images of an s orbital representation of the tip at shorter tip–surface distance by about 1 Å.

A more "typical" tip was prepared by bringing a tungsten tip in contact with the copper surface and was therefore composed of copper and tungsten. The aquired profiles with this tip are also shown in Figure 12. Because the exact nature of the "typical" and "sharp" tips is unknown, we will compare the measured STM profiles for both types of tips with the calculated LDOS profiles using an s representation of the tip. What emerges is a complementary relationship between the calculated tip–surface distances and the perceived image resolution.

As shown in Figure 12, all characteristic features of the STM profiles for the three chemisorbed molecules obtained using the

"sharp" tip are reproduced in detail with the calculated LDOS profiles at z_0 in the range of 5−6 Å. For the chemisorbed C$_2$H$_2$ and C$_2$, the magnitude and the shape of the two protrusions are reproduced quantitatively at $z_0 = 5$ Å. In the case of the chemisorbed C$_2$H, we get a similar agreement between theory and experiment at $z_0 = 6$ Å except that the calculated LDOS gives a small depression at $d_{[\bar{1}10]} \sim 3.5$ Å, which is not resolved in the measured STM profile. The good agreement between calculated LDOS profiles and measured STM profiles using the "sharp" tip demonstrates the utility of coupling density functional theory with the Tersoff−Hamann approximation. In addition, our analysis of the calculated LDOS profiles in section 3.4 revealed the expected physical content of the theory: the characteristic protrusions of the measured STM profiles derive from molecular orbitals that participate in the chemisorption bond.

STM profiles for each of the three chemisorbed molecules obtained by the "typical" tip at large gap resistance exhibit a rather nonspecific depression (Figure 12). The spatial extent and magnitude of this depression for each chemisorbed molecule is reproduced by the calculated STM profiles with a large gap z_0 of about 10 Å. For such large z_0, the lateral size of the 4 × 4 surface unit cell ($\sim$10 Å) is becoming too small to accurately represent isolated adsorbates. The earlier LDOS analysis showed that such a depression should be dominant for an electronegative adsorbate imaged at large z_0. The depression arises from two related effects of chemisorption: the transfer of electrons from Cu free-electron-like states into more localized states derived from molecular orbitals and the subsequent screening of this transferred charge by conduction electrons.

The good agreement obtained for these specific molecules is indicative of a more general conclusion: STM images taken at large tip–sample distances will reflect long-wavelength disturbances of the substrate states. As the tip–surface distance is decreased, a larger fraction of the LDOS is comprised of more localized contributions from states that can be associated with specific molecular orbitals. A key point of this paper is that these qualitative expectations are confirmed in a quantitative way by application of the Tersoff−Hamann approximation to DFT, thereby coupling the physical insights of more qualitative methods with the accuracy of DFT calculations.

For a "typical" tip, some of us have earlier reported STM images for C$_2$H$_2$ chemisorbed on Cu(001)[45,46,47] showing features reminiscent of those present in the STM profiles of the "sharp" tip of the present manuscript. These features consist of two protrusions with a pronounced depression in between. The values of 0.23 and 5 Å for the maximum depth of the depression and the distance between the protrusions, respectively, in the STM image in ref 46 are well reproduced by the calculated LDOS profile in Figure 9b,c at $z_0 = 8$ Å. It is worth noting that when the "typical" tip of the current work is moved $\sim$2 Å closer to the surface by imaging at a higher current level, the protrusions characteristic of previously published images are recovered.[48] Thus, the conclusions reached by applying the theory to cases of "sharp" and "typical" tips are in agreement with trends in the distance-dependent images of a "typical" tip alone.[49]

It is not straightforward to determine whether the tip–surface distances for the calculated profiles are in agreement with the true tip–surface distances in the corresponding experimental images. The calculations suggest that the tip–surface distance for "sharp" tips is less than that for "typical" tips. This is quite consistent with the following experimental observation: the distance toward the surface that the tip must be advanced to

make an observable change in the surface (i.e., to make contact) is smaller for tips that exhibit large corrugation than for tips that exhibit poor resolution. This provisional definition of surface contact produces a tip−surface distance that is in the range 6−10 Å, which is comparable to the calculated tip−surface distances.

We have estimated the tunneling resistances in the tip model introduced by Stokbro and co-workers[25] to obtain additional, though indirect, information about z_0. In this model, the tip is modeled by an adsorbed W atom on a W(110) surface where the projected DOS on the W tip atom s orbital was calculated using DFT.[50] This model gives a tunneling resistance that increases exponentially from ∼0.5 MΩ at $z_0 = 5$ Å to ∼5 GΩ at $z_0 = 9$ Å. The measured tunneling resistances of 5 GΩ for the "normal" tip are consistent with the results of this model for the range of $z_0 = 9-10$ Å that reproduced the measured STM images. The tunneling resistances at $z_0 = 5-6$ Å, which gave LDOS images that were in agreement with the STM images obtained by the "sharp" tip, are harder to reconcile with the measured tunneling resistances in the range of 50 MΩ to 5 GΩ. A better agreement between measured resistances and calculated resistances corresponding to matching LDOS profiles is obtained with a p_z state representation of the tip, which is more appropriate for a tip terminated by a S atom. In this case, the calculated LDOS images are in agreement with the observed STM images at $z_0 = 6-7$ Å for which we find the tunneling resistance to be in the range 4−40 MΩ. Given that the gap resistance varies by an order of magnitude per Å both theoretically and experimentally, the agreement achieved here is satisfactory.

5. Summary and Concluding Remarks

We have carried out density functional theory calculations of STM images of acetylene, ethynyl, and dicarbon chemisorbed on the (001) surface of copper using the Tersoff−Hamann approximation for tunneling. The calculated topographic images of the local density of states at the Fermi level were compared directly with constant-current STM images obtained with a metallic tip and a chemically modified tip. We find that the Tersoff−Hamann approximation for calculation of STM images using the Kohn−Sham wave functions of the DFT calculations reproduces the experimental STM images and provides a most useful basis for the understanding of STM images of chemisorbed molecules. The images of the chemisorbed hydrocarbon molecules obtained by the functionalized tips exhibited characteristic features that were shown to derive from molecular orbitals that participate in the chemisorption bond. At larger tip−surface distances, we find that the LDOS images evolve into rather nonspecific depressions in agreement with experimental STM images obtained using typical tips at large distances. This type of depression should prove a common phenomenon for electronegative adsorbates as it arises from two general effects: the transfer of electrons from free-electron-like states to the chemisorbed molecule and the screening of these adsorbate-induced states by the itinerant electrons. The calculated chemisorption parameters such as bonding geometry and vibrational energies are in good agreement with available experimental data.

Note Added after Print Publication. Figures 7, 9, 10, and 11, originally published in black and white, are given here in color. This article was published on the Web 7/16/2002 and in the special issue "John C. Tully Festschrift" (**2002**, *106*, 8161). An Addition and Correction appears in the October 24, 2002 issue.

References and Notes

(1) Hahn, J. R.; Lee, H. J.; Ho W. *Phys. Rev. Lett.* **2000**, *85*, 1914.

(2) Tersoff, J.; Hamann, D. R. *Phys. Rev. Lett.* **1983**, *50*, 1998.

(3) Lang, N. D. *Phys. Rev. Lett.* **1986**, *56*, 1164.

(4) Sautet, P.; Joachim, C. *Chem. Phys. Lett.* **1991**, *185*, 23.

(5) Chen, C. J. *Phys. Rev. B* **1990**, *42*, 8841.

(6) Doyen, G.; Drakova, D.; Scheffler, M. *Phys Rev. B* **1993**, *47*, 9778.

(7) Sautet, P. *Chem. Rev.* **1997**, *97*, 1097.

(8) Hofer, W. A.; Redinger, J. *Surf. Sci.* **2000**, *447*, 51.

(9) Bocquet, M. L.; Sautet, P. *Phys. Rev. B* **1999**, *59*, 15437.

(10) Eichler, A.; Mittendorfer, F.; Hafner, J. *Phys. Rev. B* **2000**, *62*, 4744.

(11) Helveg, S.; Lorensen, H. T.; Horch, S.; Laesgaard, E.; Stensgaard, I.; Jacobsen, K. W.; Norskov, J. K.; Besenbacher, F. *Phys. Rev. B* **1998**, *58*, 16432.

(12) Chen, M.; Clark, P. G.; Mueller, Jr. T.; Friend, C. M.; Kaxiras, E. *Phys. Rev. B* **1999**, *60*, 11783.

(13) Lorente, N.; Persson, M. *Phys. Rev. Lett.* **2000**, *85*, 2997.

(14) Yuan, L.-F.; Yang, J.; Li, Q.; Zhu, Q.-S. *J. Chem. Phys.* **2002**, *116*, 3104.

(15) Hansen, L.; et al. *Dacapo* 1.30; DACAPO is developed and maintained by Center for Atomic Scale Materials Physics (CAMP), Denmark Technical University, Denmark.

(16) Perdew, J. P.; Chevary, J. A.; Vosko, S. H.; Jackson, K. A.; Pedersen, M. R.; Singh, D. J.; Fiolhais, C. *Phys. Rev. B* **1992**, *46*, 6671.

(17) The slab contained four layers of Cu atoms, and the vacuum region contained five empty layers.

(18) Vanderbilt, D. *Phys. Rev. B* **1990**, *41*, 7892.

(19) The plane wave cutoff energy was 30 Ry. The surface Brillouin zone (SBZ) for the (3×3) and the (4×4) surface unit cells was sampled uniformly by either 9 or 16 k points.

(20) Lorente, N.; Persson, M. *Faraday Discussions* **2000**, *117*, 277.

(21) The root-mean-square (rms) width is given by $\sigma/(2)^{1/2}$.

(22) The calculated pseudo wave functions $\psi_{n\mathbf{k}}(\mathbf{r})$ was extended analytically from a plane well outside the ion-cores to the remote tip region by assuming that the one-electron potential is zero in this region.[23,24]

(23) Sacks, W.; Gauthier, S.; Rousset, S.; Klein, J.; Esrick, M. A. *Phys. Rev. B* **1987**, *36*, 961.

(24) Heinze, S.; Blügel, S.; Pascal, R.; Bode, M.; Wiesendanger, R. *Phys. Rev. B* **1998**, *58*, 16432.

(25) Stokbro, K.; Quade, U.; Grey, F. *Appl. Phys. A* **1998**, *66*, S907.

(26) Desjonquéres, M. C.; Spanjaard, D. *Concepts in surface physics*; Springer-Verlag: Berlin, 1996.

(27) Davis, H. L.; Noonan, J. R. *J. Vac. Sci. Technol.* **1982**, *20*, 842.

(28) Lauhon, L. J.; Ho, W. *J. Phys. Chem.* **2001**, *104*, 3987.

(29) Arvanitis, D.; Wenzel, L.; Baberschke, K. *Phys. Rev. Lett.* **1987**, *59*, 2435.

(30) F. Johansson, *A quantum mechanical study of the hydrogen atom motion on a Cu(100) surface and comparison with experiments*; M.Sc. Thesis, Chalmers University of Technology, Göteborg; Applied Physics Report no. 2000-100, 2000.

(31) Lauhon, L.; Ho, W. *J. Chem. Phys.* **1999**, *111*, 5633.

(32) Lauhon, L.; Ho, W. *Surf. Sci.* **2000**, *451*, 219.

(33) Herzberg, G. *Molecular structure and molecular spectra*; Van Nostrand: New York, 1950.

(34) Huber, K. P.; Herzberg, G. *Molecular structure and molecular spectra IV. Constants of diatomic molecules*; Van Nostrand: New York, 1950.

(35) Our DFT calculation gives a $^1\Sigma_g^+$ ground state for the free C_2 molecule, in contrast to the experimental ground state which is $^3\Pi_u$.[33] The reason lies in the small energy difference between the π_u and σ_g orbitals and the approximate treatment of exchange and correlation in our calculation.

(36) Hoffmann, R. *Rev. Mod. Phys.* **1988**, *60*, 601.

(37) Hoffman, D. M.; Hoffmann, R.; Fisel, C. R. *J. Am. Chem. Soc.* **1982**, *104*, 3858.

(38) Lang, N. D.; Williams, A. R. *Phys. Rev. B* **1978**, *18*, 616.

(39) Lang, N. D. *Surf. Sci* **1983**, *127*, L118.

(40) Jacox, M. E.; Olson, W. B. *J. Chem. Phys* **1987**, *86*, 3134.

(41) Marinova, Ts. S.; Stefanov, P. K. *Surf. Sci.* **1987**, *191*, 66.

(42) Stipe, B. C.; Rezaei, M. A.; Ho, W. *Phys. Rev. Lett.* **1999**, *82*, 1724.

(43) Klink, C.; Olsen, L.; Lang, N. D. *Phys. Rev. Lett.* **1993**, *71*, 4350.

(44) Lang, N. D. *Comments Cond. Mater. Phys* **1989**, *14*, 253.

(45) Lauhon, L.; Ho, W. *Phys. Rev. Lett.* **2000**, *84*, 1527.

(46) Stipe, B. C.; Rezaei, M. A.; Ho, W. *Science* **1998**, *280*, 1732.

(47) Stipe, B. C.; Rezaei, M. A.; Ho, W. *Phys. Rev. Lett.* **1998**, *81*, 1263.

(48) Note that the smaller 3 × 3 unit cell used previously in ref 13 required a somewhat larger z_0 of about 9.5 Å for the background to reproduce the observed corrugation parameters.

(49) Typical tips cannot produce arbitrarily high resolution. The tunneling conditions required to reduce the tunneling gap eventually result in physical instability of the tip or sample.

(50) The projected DOS was calculated to be $\rho_s(\epsilon_F) = 0.0135$ eV Å^{-3}, and the effective radius of curvature R was 1.59 Å, which gave $C_s = $ eVÅ^3/Ω. Note that Tersoff and Hamann suggested a value for C_s that results in tunneling resistances that are about 14 times smaller than suggested by this model.

(51) Bogey, M.; Demuynck, C.; Destombes, J. L. *Mol. Phys.* **1989**, *66*, 955.

(52) Strey, G.; Mills, I. M. *J. Mol. Spectrosc.* **1976**, *59*, 103.

(53) Urdahl, R. S.; Bao, Y.; Jackson, W. M. *Chem. Phys. Lett.* **1991**, *278*, 4255.

(54) Wagman, D. D.; Parker, V. B.; Schuman, R H.; Halow, I.; Bailey, S. M.; Churney, K. L.; Nuttall, R. L. *J. Chem. Phys. Ref. Data* **1982**, *11*, Suppl. 2.